

Quantum-inspired activation functions in the convolutional neural network

Shaozhi Li^{1,*}, M Sabbir Salek^{1,2}, Yao Wang³, and Mashrur Chowdhury^{1,2}

¹National Center for Transportation Cybersecurity and Resiliency (TracR), Clemson University, SC 29631, USA

²Glenn Department of Civil Engineering, Clemson University, Clemson, SC 29634, USA

³Department of Chemistry, Emory University, Atlanta, GA 30322, USA

*lishaozhiphys@gmail.com

ABSTRACT

Driven by the significant advantages offered by quantum computing, research in quantum machine learning has increased in recent years. While quantum speed-up has been demonstrated in some applications of quantum machine learning, a comprehensive understanding of its underlying mechanisms for improved performance remains elusive. Our study fills this gap by examining the expressibility of quantum circuits integrated within a convolutional neural network (CNN). Through numerical training on the MNIST dataset, our hybrid quantum-classical CNN model exhibited superior feature selection capabilities and significantly reduced the required training steps compared to the classical CNN. To understand the root of this enhanced performance, we conducted an analytical investigation of the functional expressibility of quantum circuits and derived a quantum activation function. We demonstrated that this quantum activation is more efficient in selecting important features and discarding unimportant information of input images. These findings not only deepen our comprehension of quantum-enhanced machine-learning models but also advance the classical machine-learning technique by introducing the quantum-inspired activation function.

Introduction

The unparalleled potential of quantum algorithms over their classical counterparts has ignited widespread enthusiasm for quantum computing^{1–10}. Thanks to the achievements in quantum hardware development^{11–15}, quantum supremacy was demonstrated via the random sampling task made by the Google superconducting quantum computer and the photonic quantum device^{16,17}. In addition to these landmark achievements, quantum computing has found applications across diverse domains, including simulating many-body Hamiltonian^{2,18–24}, simulating spectroscopies^{25–29}, and solving NP-complete problems^{30–34}. Among them, most of these applications use the variational technique to find a solution with a minimal value of the loss function or the energy, which is analogous to the strategy used in machine learning techniques, inspiring the idea of quantum machine learning^{35,36}.

The current extensively used supervised quantum machine learning methods use quantum models or circuits to extract essential features^{37–42}. Unlike the kernel method used in classical machine learning, the quantum model encodes data in the high-dimensional Hilbert space and utilizes a series of quantum gates to construct nonlinear quantum kernel functions. Broadly, these quantum kernel methods fall into two categories: explicit and implicit quantum models⁴³. Explicit models utilize measurements of a quantum state controlled by encoded data and parameterized gates. The recently proposed data reuploading model also belongs to this category^{44,45}. Implicit models weigh the inner products

of quantum states controlled by the encoded input data. A representative example of the implicit model is the quantum support vector machine^{46–50}. Compared to implicit models, explicit models create more complex functions, posing significant challenges to our understanding, which in turn obscures the mechanisms underpinning their superior performance in some case studies^{51–57}.

Understanding the origin of superior performance in quantum machine learning is essential for optimizing quantum models and potentially enriching classical algorithms. Quantum-inspired classical algorithms, for example, have already accelerated linear algebra computations, showcasing the benefits of translating quantum insights to classical contexts^{58–61}. Despite these advancements, the machine learning field sees a paucity of quantum-inspired algorithms, primarily due to an inadequate grasp of quantum model intricacies⁶². This knowledge gap has spurred investigations into the expressibility of quantum models^{63–66}. However, giving an analytical relationship between the expressibility and the architecture of a quantum circuit is challenging, and this difficulty increases with the number of qubits and quantum gates. Consequently, research has predominantly pursued numerical evaluations, including evaluating the expressibility of the Hilbert space and the functional expressibility^{63–66}. For instance, the expressibility of the Hilbert space was characterized by comparing different distributions of the fidelity between the quantum state from a quantum model and the Haar-random states⁶³. In addition, it was proposed to understand the functional expressibility of a quantum model by utilizing the Fourier series⁶⁴. While these insights advance our understand-

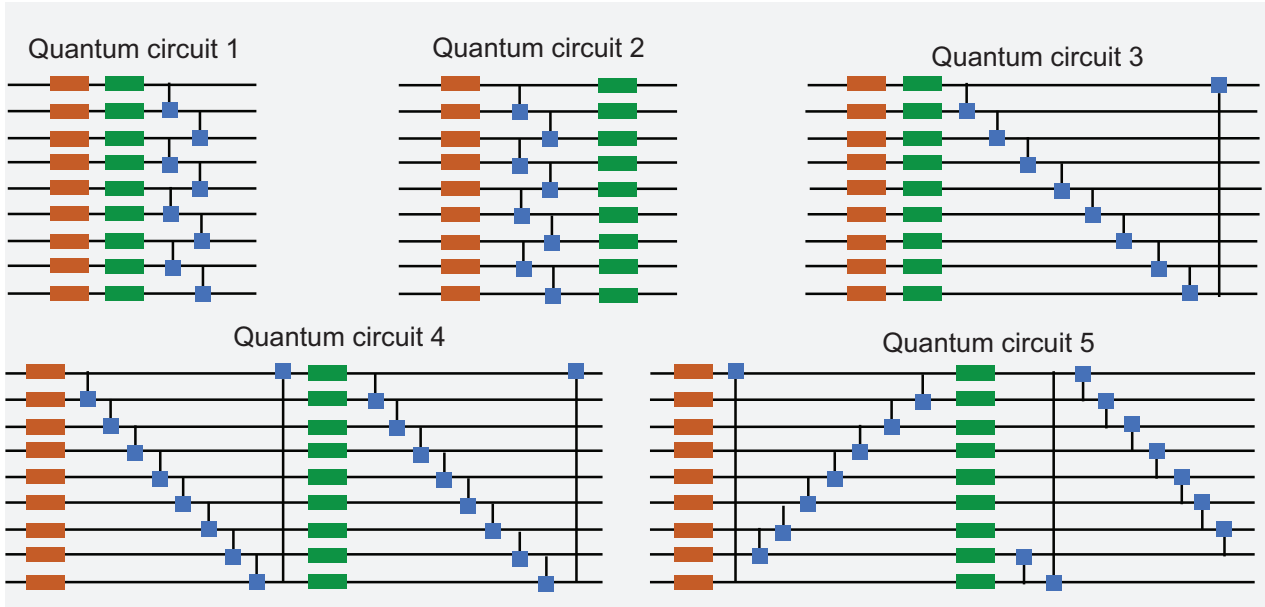


Figure 1. Five quantum circuits used in our study. The orange- and green-colored rectangles represent parametric R_y rotation operators. In circuits 2, 4, and 5, these two R_y operators are separated by a CNOT gate. In circuit 1 and circuit 3, two R_y operators are applied one after another, which can be merged into a single R_y operator.

ing, they fail to elucidate the relationship between Hilbert space expressibility and quantum machine learning efficacy. Moreover, the decomposition of a function into a Fourier series cannot intuitively reflect the nonlinear relationship between the input data and the output. To advance quantum machine learning techniques, it is vital to address these foundational questions.

Our research advances the understanding of quantum models in quantum machine learning by providing clear, analytical expressions for quantum circuits, setting our work apart from prior studies. Specifically, we analyze five shallow quantum circuits integrated within a convolutional neural network (CNN) framework. To compare the hybrid convolutional neural network (CNN) and the classical CNN, we restrict ourselves to the situation that these five quantum models have the same number of variables as that in the classical CNN. To understand the trainability of these circuits, we first study the expressibility of the Hilbert space of these circuits and observe a similar expressibility and trainability among these five circuits. We then explore the training speed of hybrid CNNs with these five quantum circuits and attribute different performances to different functional expressibilities. A notable discovery is that circuits employing a rotation operator directly after the data upload via angle encoding outperform those incorporating a CNOT layer between the data encoding and rotation operations. This insight is instrumental for optimizing quantum circuit design in hybrid systems. Further, we succeeded in deriving analytical expressions of the quantum circuit yielding the best performance in the hybrid CNN, which is char-

acterized as a continued product of the cosine series. Compared to the traditional Tanh and Sigmoid activation functions, this quantum activation function can efficiently select essential features and discard unimportant information, resulting in faster loss function convergence. This finding is pivotal because we offer a clear explanation for the superior performance of hybrid CNNs and a quantum-inspired activation function with enhanced efficiency to the broader machine-learning community.

Results

Quantum Circuits

Our study aims to elucidate the performance of hybrid quantum-classical machine learning frameworks with different quantum models. To avoid the quantum barren plateau⁶⁷, we focus on five shallow quantum circuits (QCs), as depicted in Fig. 1. In QCs 1 and 3, sequential parametric R_y rotation operators—represented as orange and green rectangles—proceed without intermediary quantum operations. Conversely, the two rotation operators are separated by a CNOT layer in QCs 2, 4, and 5 (QC 5 is investigated in Ref. 63). These five circuits have different architectures, generating different expressibilities of the Hilbert space and functional expressibilities. As discussed in early studies^{63,65}, these two expressibilities could affect the performance of the hybrid quantum-classical neural network, although the hidden mechanism is unclear. To explore this relationship, we will integrate these quantum models into a CNN.

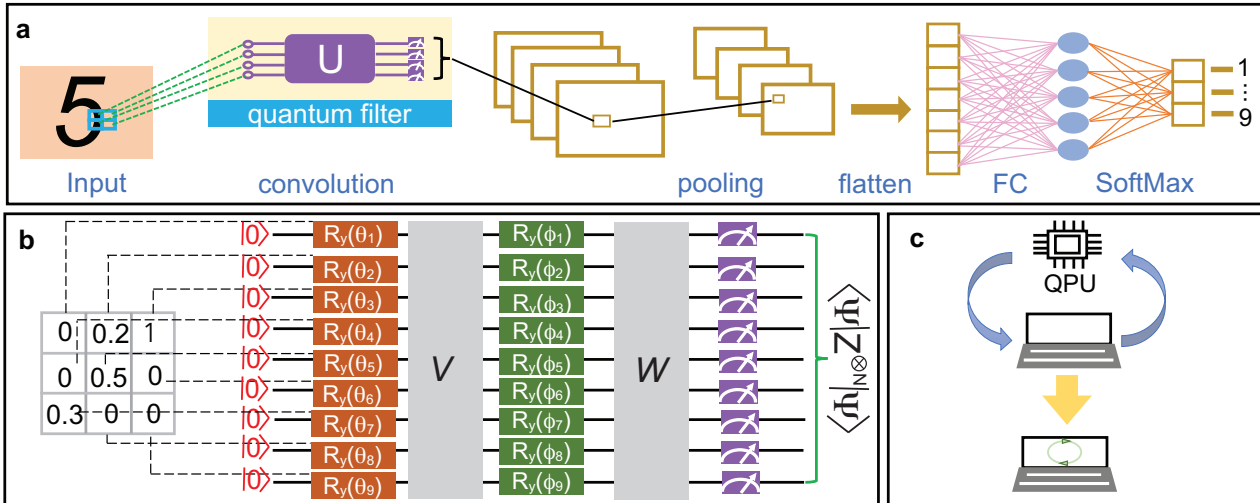


Figure 2. Hybrid quantum-classical convolutional neural network (CNN). **a**, A figure for the hybrid CNN architecture, which includes one convolution layer, one average pooling layer, one flattened layer, and two fully connected (FC) neural networks. **b**, A quantum circuit with nine qubits is sketched. **c**, A figure for advancing the classical machine learning method via quantum-inspired algorithms.

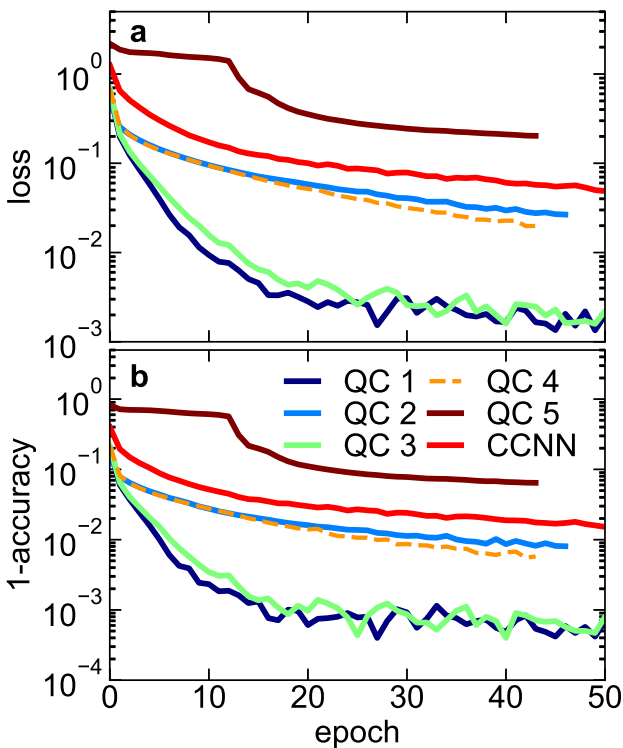


Figure 3. The performance of the hybrid convolutional neural network (CNN) and the classical CNN. The top panel plots the loss function at each epoch during the training phase. The bottom panel plots the training accuracy. The MNIST dataset with 57,600 samples is used to train these CNN models.

Before performing a machine learning task, we need to understand the trainability of these quantum circuits, which can be characterized by the expressibility of the Hilbert space. The relationship between the trainability and the expressibility was explained in Ref. 68, which concluded that a quantum circuit with strong expressibility of the Hilbert space exhibits the quantum barren plateau issue, leading to a weak trainability. To quantize the expressibility of the Hilbert space of a quantum circuit, we follow Ref. 63 and compare the distribution of quantum states obtained from sampling the parameters of a quantum circuit to the uniform distribution of Haar-random states. The Kullback-Leibler (KL) divergence is used to characterize different distributions of the fidelity of these quantum states (see details in the method section). A smaller value of KL divergence denotes a better expressibility of the Hilbert space. It is found that these five circuits generate a similar distribution of fidelities, leading to a comparable value of KL divergence, which is about 0.345 (see Supplementary Note 1). This result implies that these five quantum circuits have a similarly limited expressibility of the Hilbert space; as a result, they exhibit good trainability⁶⁸.

Hybrid quantum-classical convolutional neural network

Although these quantum circuits have similar expressibility of the Hilbert space and trainability, they have different functional expressions, leading to different performances of the hybrid machine learning approach. Here, we focus on the example of the hybrid quantum-

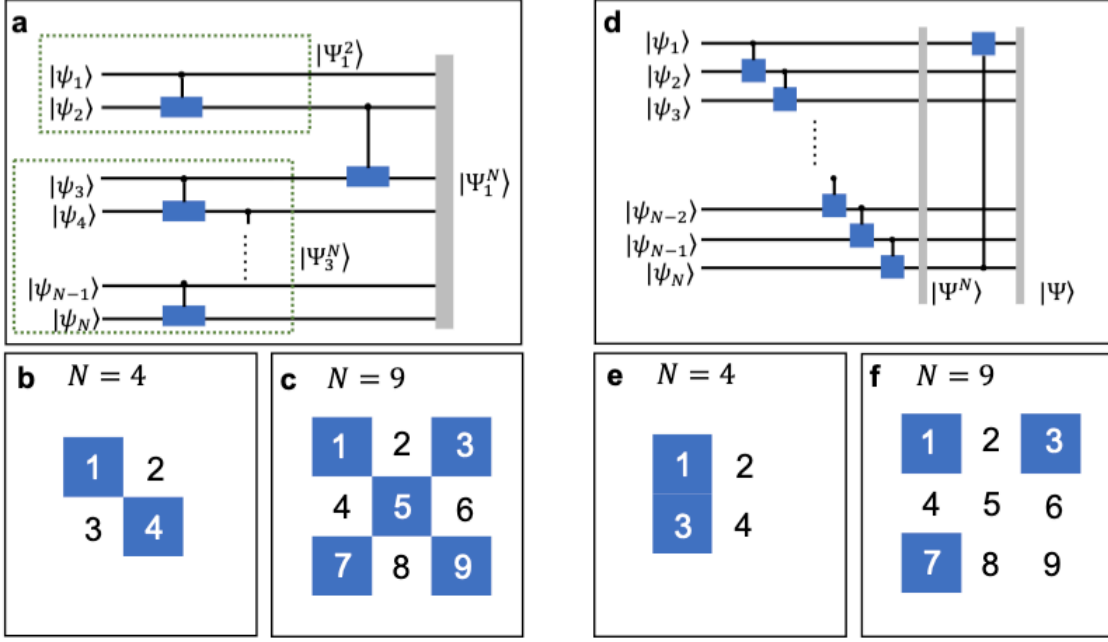


Figure 4. Analysis of Quantum Circuits. **a**, The quantum state $|\Psi_1^N\rangle$ of quantum circuit 1 is divided into two parts, $|\Psi_1^2\rangle$ and $|\Psi_3^N\rangle$, where N is the total number of qubits. **b**, The contribution of a 2×2 filter encoded into quantum circuit 1 comes from the first and fourth qubits. **c**, The contribution of a 3×3 filter encoded into quantum circuit 1 comes from qubits with odd indexes. **d**, The analysis of quantum circuit 3. **e**, The contribution of a 2×2 filter encoded into quantum circuit 3 comes from the first and third qubits. **f**, The contribution of a 3×3 filter encoded into quantum circuit 3 comes from the first, third, and seventh qubits.

classical CNN. As shown in Fig. 2a, our hybrid CNN includes one convolutional layer with quantum filters, one average pooling layer, one flattened layer, and two fully connected (FC) neural networks (NN). We define the number of features within the first hidden layer as L and set the number of neurons in the last-second hidden layer as $L_2 = 2L$. For the output layer, a SoftMax activation function is employed to facilitate multi-class classification (10 classes are used in our simulations) alongside the use of a categorical cross-entropy loss function.

The architecture of the quantum filter is delineated in Fig. 2b. For each quantum circuit, we encode an $N_x \times N_y$ patch ($x_{i,j}$) of the input image into a quantum state by setting the rotation angle in the first R_y rotation layer as $\theta_{i \times N_y + j} = x_{i,j} \times \pi$. The notations W and V are utilized to denote the controlled-NOT (CNOT) layer within our quantum circuits. When the CNOT layer is omitted between successive R_y operators, V is substituted by an identity operator. The angle applied to the subsequent R_y operator is a parametric variable, which is used to minimize the loss function. The neuron in the first hidden layer corresponds to the output of the quantum circuit, which is the expectation value of $Z^{\otimes N}$, where N represents the number of qubits, and Z denotes the z-component of the Pauli matrix. Notably, the number of parametric variables within our hybrid CNN aligns with its classical

counterpart, except for the biased variable. This configuration facilitates a direct comparison between hybrid and classical CNNs.

We use the MNIST dataset to train our models with $L = 16$ and a batch size of 64⁶⁹. In our work, the training sample size is 57,600, and the testing sample size is 10000. As depicted in Fig. 3, the evolution of the loss function and the accuracy at each epoch during the training phase is plotted for both the five hybrid CNNs and the classical CNN (CCNN). Notably, the analysis reveals that the hybrid CNNs employing quantum circuits 1 and 3 exhibit a markedly accelerated decrease in both the loss function and the residue of the accuracy (defined as 1-accuracy) compared to their counterparts. Hybrid CNNs with QC 2 and 4 have similar performances and are trained slightly faster than the classical CNN. For the hybrid CNN with QC 5, the loss function and the residue of the accuracy decrease slower than the classical CNN. The better performances of the hybrid CNNs with QCs 1 and 3 show that re-rotating the encoded angle makes better feature selections, which is attributed to the neural network model optimizing the encoding method. In addition, we note that the complex function generated by quantum circuits does not always guarantee a better performance.

The different training speeds among these five hybrid CNNs are attributed to distinct functional expressions of

these quantum circuits. To uncover the roots of these variations, we conduct a detailed study of their analytical expressions.

Quantum Circuit 1

We start our analysis with quantum circuit 1. To obtain the output $\langle \Psi | Z^{\otimes N} | \Psi \rangle$ of QC 1, we need to use the following proposition. Here, $|\Psi\rangle$ is the final quantum state of this quantum circuit.

Proposition 1 *We consider a quantum circuit composed of N qubits, where the initial state $|\psi_i\rangle$ of each qubit is described by $|\psi_i\rangle = q_i|0\rangle + p_i|1\rangle$. Upon the application of a CNOT gate between two adjacent qubits first across even-indexed qubits and then odd-indexed qubits, as depicted in Fig. 4a, the expectation value of the operator $Z^{\otimes N}$ is determined by the following recursive relationship:*

$$\langle \Psi_1^N | Z^{\otimes N} | \Psi_1^N \rangle = [|p_1|^2 - |q_1|^2] \times \langle \Psi_3^N | Z^{\otimes N-2} | \Psi_3^N \rangle, \quad (1)$$

where $|\psi_n^m\rangle = \otimes_{i=n}^{i=i+2, i < m} CX(i, i+1) \otimes_{j=n+1}^{j=j+2, j < m} CX(j, j+1) \otimes_{i=n}^m |\psi_i\rangle$. The notation $CX(i, j)$ denotes a CNOT gate with qubit i as the controller and qubit j as the target.

To demonstrate this proposition, we treat the first two qubits and the remaining qubits, shown in Fig. 4a, separately. The quantum state on the first two qubits after applying a CNOT gate is

$$|\Psi_1^2\rangle = q_1 q_2 |00\rangle + q_1 p_2 |01\rangle + p_1 q_2 |11\rangle + p_1 p_2 |10\rangle. \quad (2)$$

We label the quantum state on the remaining $N-2$ qubits as $|\Psi_3^N\rangle$ and entangle this state with $|\Psi_1^2\rangle$ via a CNOT gate $CX(2, 3)$. The entangled quantum state is then given by

$$|\Psi_1^N\rangle = [q_1 q_2 |00\rangle + q_1 p_2 |01\rangle X_3 + p_1 q_2 |11\rangle X_3 + p_1 p_2 |10\rangle] \otimes |\Psi_3^N\rangle. \quad (3)$$

Here, X_3 is the x -component Pauli matrix that acts on the third qubit. Utilizing the relationship that $\langle \Psi_3^N | X_3 Z^{\otimes N-2} X_3 | \Psi_3^N \rangle = -\langle \Psi_3^N | Z^{\otimes N-2} | \Psi_3^N \rangle$, we find

$$\langle \Psi_1^N | Z^{\otimes N} | \Psi_1^N \rangle = [|p_1|^2 - |q_1|^2] \langle \Psi_3^N | Z^{\otimes N-2} | \Psi_3^N \rangle. \quad (4)$$

Proposition 1 is demonstrated from the above derivations. With proposition 1, we can easily obtain the output of QC 1. If the number of qubits N is odd, the output is $\langle \Psi_1^N | Z^{\otimes N} | \Psi_1^N \rangle = -\prod_{i \in \text{odd}}^N [|p_i|^2 - |q_i|^2]$; if N is even, then the output becomes $\langle \Psi_1^N | Z^{\otimes N} | \Psi_1^N \rangle = -[|p_N|^2 - |q_N|^2] \times \prod_{i \in \text{odd}}^{N-3} [|p_i|^2 - |q_i|^2]$. In QC 1, p_i and q_i depend on the values of θ_i and ϕ_i . With some effort, we find that the output of QC 1 can be written as

$$f_{QC1}(\theta, \phi) = \begin{cases} -\prod_{i \in \text{odd}}^N \cos \alpha_i & N \in \text{odd} \\ -\cos \alpha_N \prod_{i \in \text{odd}}^{N-3} \cos \alpha_i & N \in \text{even} \end{cases} \quad (5)$$

where $\alpha_i = \theta_i + \phi_i$. Equation (5) shows that the output of QC 1 depends on rotation angles on specific qubits. For

example, the output of a 2×2 quantum filter depends on the angle on the first and fourth qubits, which are highlighted by the blue color in Fig. 4b. For a 3×3 filter, the output is determined by the angle on the qubit with odd indexes (see Fig. 4c).

Quantum Circuit 3

Our investigation into the activation function of QC 3 commences by examining the quantum state prior to the final CNOT gate application, denoted as $|\Psi^N\rangle$, and illustrated in Fig. 4d. Proposition 2 provides the necessary framework for this analysis, establishing that $|\Psi^N\rangle$ can be succinctly described through a recursive formulation, detailed as follows.

Proposition 2 *Upon the application of a CNOT gate between adjacent qubits within a quantum circuit starting from the initial state $|\psi_i\rangle$ of each qubit, the resultant quantum state evolves into*

$$|\Psi^N\rangle = [p_N |g^{N-2}\rangle \otimes |0\rangle_{N-1} + q_N |t^{N-2}\rangle \otimes |1\rangle_{N-1}] \otimes |0\rangle_N + [q_N |g^{N-2}\rangle \otimes |0\rangle_{N-1} + p_N |t^{N-2}\rangle \otimes |1\rangle_{N-1}] \otimes |1\rangle_N, \quad (6)$$

where $|g^{N-2}\rangle$ and $|t^{N-2}\rangle$ represent states across the first $N-2$ qubits. These two quantum states follow recursion relationships, which are expressed as

$$|g^{N-2}\rangle = p_{N-2} |g^{N-4}\rangle \otimes |0\rangle_{N-3} + q_{N-2} |t^{N-4}\rangle \otimes |1\rangle_{N-3}, \quad (7)$$

$$|t^{N-2}\rangle = q_{N-2} |g^{N-4}\rangle \otimes |0\rangle_{N-3} + p_{N-2} |t^{N-4}\rangle \otimes |1\rangle_{N-3}. \quad (8)$$

Utilizing the relationship between the output wavefunction $|\Psi\rangle$ of QC 3 and $|\Psi^N\rangle$ and Eq. (6), the output $\langle \Psi | Z^{\otimes N} | \Psi \rangle$ of QC 3 can be represented by $|g^{N-2}\rangle$ and $|t^{N-2}\rangle$ via

$$\langle \Psi | Z^{\otimes N} | \Psi \rangle = \langle g^{N-2} | Z^{\otimes N-2} | g^{N-2} \rangle - \langle t^{N-2} | Z^{\otimes N-2} | t^{N-2} \rangle. \quad (9)$$

Therefore, to obtain the result of $\langle \Psi | Z^{\otimes N} | \Psi \rangle$, we first need to evaluate $\langle g^{N-2} | Z^{\otimes N-2} | g^{N-2} \rangle$ and $\langle t^{N-2} | Z^{\otimes N-2} | t^{N-2} \rangle$. It is found that $\langle g^{N-2} | Z^{\otimes N-2} | g^{N-2} \rangle$ and $\langle t^{N-2} | Z^{\otimes N-2} | t^{N-2} \rangle$ follow the following two recursion equations,

$$\begin{aligned} \langle g^{N-2} | Z^{\otimes N-2} | g^{N-2} \rangle + \langle t^{N-2} | Z^{\otimes N-2} | t^{N-2} \rangle = \\ \langle g^{N-4} | Z^{\otimes N-4} | g^{N-4} \rangle - \langle t^{N-4} | Z^{\otimes N-4} | t^{N-4} \rangle, \end{aligned} \quad (10)$$

and

$$\begin{aligned} \langle g^{N-2} | Z^{\otimes N-2} | g^{N-2} \rangle - \langle t^{N-2} | Z^{\otimes N-2} | t^{N-2} \rangle = \\ \cos \alpha_{N-2} [\langle g^{N-4} | Z^{\otimes N-4} | g^{N-4} \rangle + \langle t^{N-4} | Z^{\otimes N-4} | t^{N-4} \rangle]. \end{aligned} \quad (11)$$

Using these recursion equations, the output of QC 3 can be formalized as

$$f_{QC3}(\theta, \phi) = \begin{cases} \left(\prod_{i=N-2}^{i=i-4, i > 4} \cos \alpha_i \right) \cos \alpha_3 \cos \alpha_1 & N = 4 + 4n \\ \left(\prod_{i=N-2}^{i=i-4, i > 6} \cos \alpha_i \right) \cos \alpha_4 \cos \alpha_2 & N = 6 + 4n \\ \left(\prod_{i=N-2}^{i=i-4, i > 5} \cos \alpha_i \right) \cos \alpha_5 \cos \alpha_2 & N = 3 + 4n \\ \left(\prod_{i=N-2}^{i=i-4, i > 5} \cos \alpha_i \right) \cos \alpha_3 \cos \alpha_1 & N = 5 + 4n, \end{cases}$$

where n is a non-negative integer. Notably, f_{QC3} also has a qubit index dependence. If we use a 2×2 quantum filter, only rotation angles on the first and third qubits contribute to the output, highlighted as blue color in Fig. 4e. For a 3×3 quantum filter, the output is determined by the rotation angle on the first, third, and seventh qubits (see Fig. 4f).

Other Quantum Circuits

Our analysis of quantum circuits 1 and 3 reveals that their activation functions can be characterized by a continued product of the cosine series. This characteristic commonly exists in QCs 2, 4, and 5. To demonstrate this argument, we will use the following proposition.

Proposition 3 Consider a quantum circuit composed of alternating layers of R_y rotation operators and CNOT gates, as depicted in Fig. 2b, the output wavefunction of the circuit for a given basis index m in the Hilbert space is formalized as:

$$|\Psi\rangle_m = \sum_{i,j,k} W_{mi} R_{i,j} V_{j,k} R_{k,0} |0\rangle, \quad (12)$$

where $W_{m,i}$ and $V_{j,k}$ are the matrix elements corresponding to the quantum layers W and V , each capable of adopting values 0 or 1. The $R_{i,j}$ denotes the matrix elements associated with the initial and subsequent rotation layers, embodying a continued product of the cosine series.

Proposition 3 is demonstrable by analyzing R_y rotation and CNOT operators. The matrix element of the R_y operator, composed of sine and cosine functions, can be uniformly expressed in cosine terms. Therefore, the matrix element of a R_y rotation layer is represented as a cosine series product. Simultaneously, the matrix elements of a CNOT operator, composed of 0 and 1, contribute to the tensor product representation of a CNOT layer. Consequently, the matrix element of a CNOT layer can only be 1 and 0. Thus, the weight of each basis of the output wavefunction $|\Psi\rangle$ is either a continued cosine product or zero, culminating in $\langle \Psi | Z^{\otimes N} | \Psi \rangle$ as a summation of these products. This characteristic persists even when more R_x and R_y rotations are added, underscoring the consistent mathematical structure of quantum activation function across various quantum circuits.

Recent advancements in quantum machine learning have concentrated on optimizing quantum circuits, as evidenced in Refs. 54, 57, 70, 71. These efforts predominantly involve simulating quantum circuits to uncover efficient pathways for hybrid machine-learning methods. Our analysis contributes to this body of knowledge by elucidating that the distinct expressions of various quantum circuits can be represented as summations over different products of cosine series. This insight facilitates a more straightforward approach by examining analytical activation functions. Compared to the complexities of

direct quantum circuit simulation, which is hampered by the exponential growth of the Hilbert space with each additional qubit, our finding offers a more accessible and scalable research alternative.

CNNs with different activation functions

Our analysis demonstrates that quantum activation functions, especially the activation functions of QCs 1 and 3, have a qubit-index or site-index dependence. To systematically assess the influence of this qubit-index dependence and its contribution to the divergent performances between classical CNNs and their hybrid counterparts, we devised an experimental framework employing five distinct activation functions (AFs), detailed in Fig. 5a. AF 1 and AF 2 incorporate the conventional Tanh function in the convolutional layer, with AF 2 introducing site dependence. AF 3 and AF 4 represent the activation functions derived from QCs 1 and 3, respectively. AF 5 adopts a site-wide product of cosine functions. In our simulations, the number of features in the first and second hidden layers are set as 16 and 64, respectively. The comparative analysis of these AFs, based on the loss function trends during the training of the MNIST dataset shown in Fig. 5b, reveals that classical CNNs with AF 1 and AF 2 exhibit analogous performance metrics, thereby indicating that site dependence does not significantly impact performance. Conversely, AFs 3, 4, and 5 showcase a markedly rapid decay in the loss function. This fast training speed is also observed in the training of the Fashion MNIST dataset, as detailed in supplementary note 4. These results strongly suggest that the accelerated training efficiency associated with AFs 3, 4, and 5 is attributed to the incorporation of higher-order nonlinearity rather than the site-dependence mechanism.

We extended our analysis to evaluate the training accuracy with these five distinct activation functions, revealing uniform performance across the training dataset for all functions. However, a discernible discrepancy was noted in the testing dataset accuracy, where models employing AF 3, AF 4, and AF 5 exhibited marginally lower scores compared to those with AF 1 and AF 2. This result suggests a subtle challenge associated with the higher-order nonlinearity introduced by the continued product of the cosine series in AFs 3, 4, and 5. To delve deeper into the potential overfitting problem, the Fashion MNIST dataset was utilized for further experimentation (detailed in supplementary note 4). The CNN model utilizing AF 3 demonstrated a notable disparity between training (99%) and testing (88%) accuracies, highlighting a pronounced overfitting concern. In contrast, the model with AF 1 maintained consistent performance across both training and testing phases, achieving an approximate accuracy (88%). Despite the overfitting observed with quantum-inspired activation functions, im-

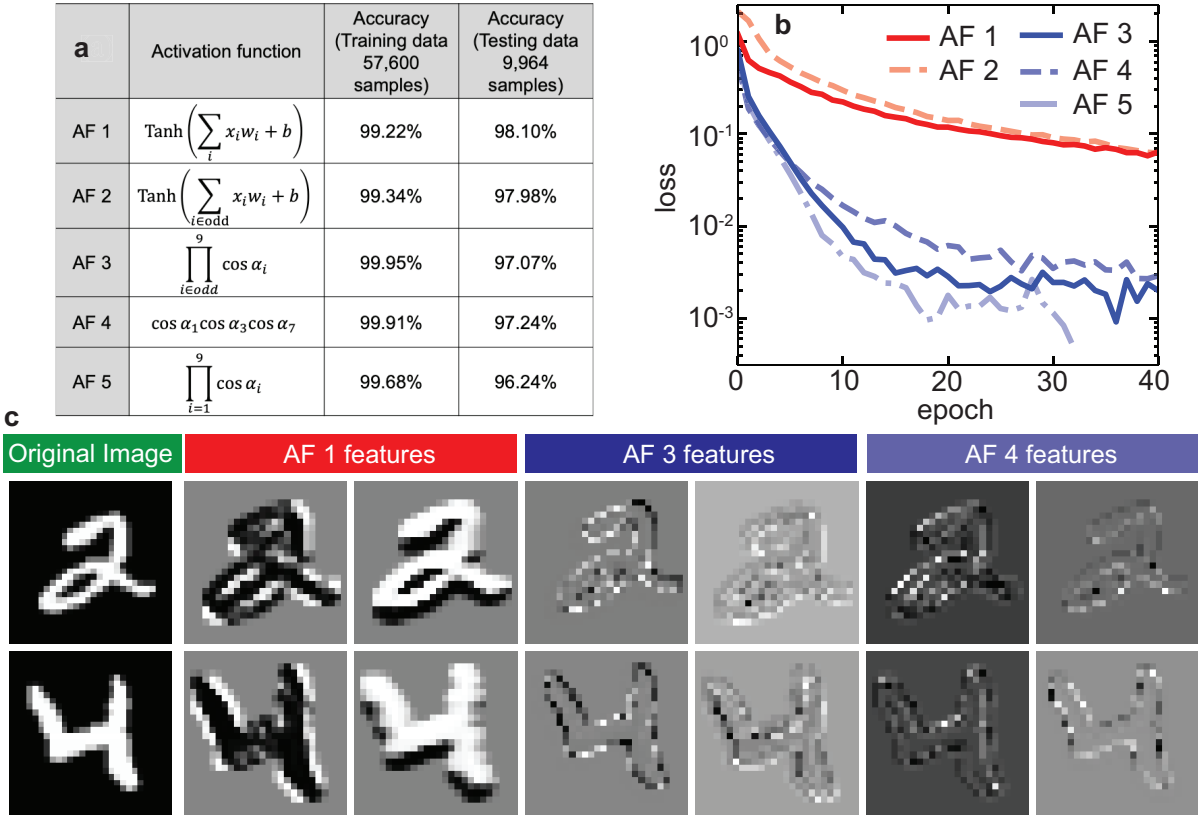


Figure 5. A comparison between different activation functions. **a**, A table contains five activation functions (AF) and the accuracies for the training data and testing data. **b**, The change of the loss function during the training phase for these five activation functions. **c**, The input image and the corresponding images in the first hidden layer for three different convolutional neural networks.

plementing an early-stop strategy proved effective in equalizing the training and testing accuracies at around 88%, thereby mitigating the overfitting issue to some extent. To demonstrate the advantage of this quantum-inspired activation function and the validity of the early-stop strategy for the overfitting issue, more case studies with different image identification datasets are required.

In addition to the rapid decrease observed in the loss function, the CNN employing the cosine function has a strong capability to select critical features from the input image. Figure 5c displays both the original images and the features extracted in the first hidden layer from CNNs with AF 1, AF 3, and AF 4. Notably, the model with AF 1 captures comprehensive detail, including both edge delineation and internal patterns within the digit imagery. In contrast, the model leveraging the cosine function primarily emphasizes edge information, which is sufficient for accurate identification. This superior feature selection by the quantum-inspired algorithm is also observed in the application to the Fashion MNIST dataset, further elucidating the advantage of cosine-based activation functions in emphasizing essential image characteristics (further details provided in supplementary note 4).

To elucidate the strong feature selection capability inherent to quantum activation functions, we explore the function $f(\alpha) = \prod_i^3 \cos \alpha_i$, where $\alpha_i = \theta_i + \phi_i$. In this formula, θ_i denotes the angle corresponding to the encoded data, and ϕ_i represents a variable. By considering a three-pixel patch as illustrated in Fig. 6a, encoding the background pixels of an image as zero yields an output of zero whenever any ϕ_i equals $\pi/2$. This zero output is similarly achieved when encoding a patch inside a digital imagery as π . At a smooth edge, where θ_i lies between 0 and π , $f(\alpha)$ is nonzero for $\phi_i = \pi/2$. Therefore, $f(\alpha)$ can distinguish the edge information and drop redundant information by setting $\phi_i = \pi/2$. We examined the trained weight ϕ_i of the CNN with AF 3, plotted in Fig. 6b. It is found that 75% of features have a weight value of $\pi/2$, denoted as a black dashed line in Fig. 6b. The remaining 25% of features have a weight value close to $\pi/2$. The deviation from $\pi/2$ of these weights is attributed to the oscillation of parameters during the training phase (see Supplementary Note 3). By tracing the evolution of weights during the training phase, we observe a convergence towards $\pi/2$ commencing from the fifth epoch. This result implies that AF3 can be eas-

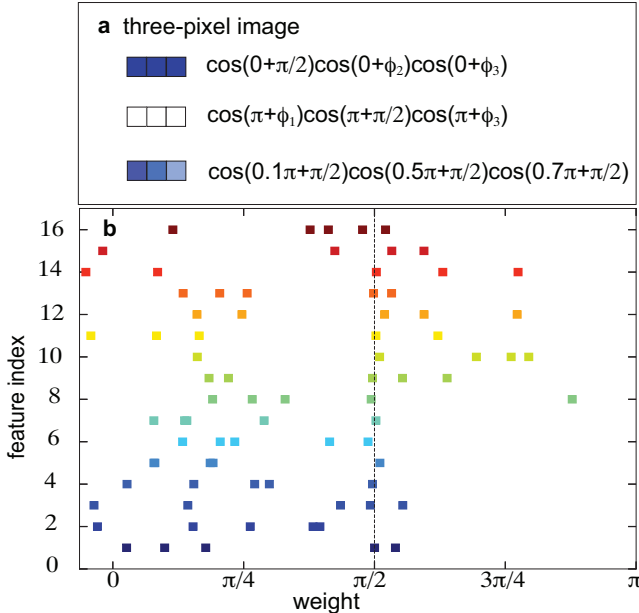


Figure 6. Analysis of the quantum-inspired activation function. **a**, A sketch of three different input patches. **b**, The distribution of trained weights across 16 features within the convolutional layer of a CNN model with activation function 3.

ily trained to distinguish the edge information, therefore resulting in a fast convergence in the loss function.

Our analysis shows that the success of the cosine-based activation function requires a smooth edge between two objects. If an image includes two objects with a clear and sharp boundary, the cosine-based activation function cannot be directly applied. In this situation, one could first apply average pooling layers to blur the boundary between two objects. For the MNIST dataset, the image resolution is low, and the edge of the digital imagery is already blurred.

Conclusion and Discussion

Our work explained how quantum circuits select features in the Hilbert space by taking examples of five shallow quantum circuits integrated into a convolutional neural network. Upon training the MNIST dataset and the Fashion MNIST dataset, we observed that the hybrid quantum-classical CNN is more efficient in selecting important features of input images compared to the classical CNN, leading to a faster convergence in the loss function. To dissect the root behind the enhanced performance of the hybrid CNN, we delve into the function expressions of quantum circuits. We demonstrated that our quantum circuits generate a polynomial function with each component being a product of the cosine series. The hybrid quantum-classical CNNs with different polynomial functions have different performances. When the

polynomial function is reduced to a monomial function, the hybrid quantum-classical CNN performs best.

To further explore the origin of the better performance of the quantum-inspired activation function, we analyze how this activation function selects features of a background patch, a patch inside digital imagery, and a patch from an edge. We demonstrate that the quantum-inspired activation function can keep essential information and discard redundant information by setting the parametric rotation angle as $\pi/2$. Importantly, this function cannot be achieved using the classical Sigmoid and Tanh activation functions.

Our training process for the hybrid quantum-classical model does not encounter the issue of quantum barren plateau⁶⁷. This phenomenon, or rather the lack thereof, can be attributed to the properties of our quantum activation function. If we consider a function $f(\alpha) = \prod_i^3 \cos \alpha_i$, the gradient of $f(\alpha)$ with respect to each angle ϕ_i is determined by the values of θ_i and ϕ_i . A scenario where the gradient is zero with a specific input patch x and ϕ_i is possible. However, this gradient shifts away from zero as the quantum filter scans across different segments of the input image, altering the input patch x . Consequently, the convolutional methodology employed here inherently precludes the persistence of zero gradients.

Our work not only deepens the understanding of quantum machine learning methods but also provides a new method for exploiting quantum supremacy. Currently, quantum machine learning has been intensively studied; however, applying this technique in quantum computers to a large dataset suffers from limited input/output bandwidth⁷² and limited quantum computing resources. Our work provides a new insight into taking advantage of quantum supremacy by finding analytical expressions of quantum circuits. Implementing these quantum-inspired activation functions in our popular machine learning software, including TensorFlow and PyTorch, is easy, and the computational cost is the same as that for the standard machine learning model. This strategy will help harness quantum supremacy through quantum-inspired classical activation functions for a broad array of machine learning application areas, including but not limited to autonomous vehicles, cybersecurity, healthcare, and finance.

Methods

Kullback-Leibler divergence

The Kullback-Leibler divergence, denoted as $D_{KL}(P||Q)$, serves as a metric for quantifying the disparity between two probability distributions: P and Q . Specifically, we employ $D_{KL}(P||Q)$ to assess the differences in the distribution of fidelities F associated with quantum states generated by a quantum circuit versus those derived from Haar-random states. The

divergence is mathematically expressed as

$$D_{\text{KL}}(P||Q) = \sum_F P(F) \log \frac{P(F)}{Q(F) + \varepsilon}, \quad (13)$$

where $\varepsilon = 10^{-20}$ is introduced to mitigate numerical instability issues. Here, $P(F)$ and $Q(F)$ respectively represent the probability distributions of the fidelity of quantum circuit states and Haar-random states.

Convolutional Neural Network

The convolutional neural network (CNN) was trained through both forward and backward propagation techniques. For the backward propagation, we computed the gradient of the loss function \mathcal{L} with respect to the rotation angle $\phi_{l,k}$ by employing the parameter shift rule, as outlined in Ref. 73. The mathematical representation is as follows:

$$\frac{\partial \mathcal{L}}{\partial \phi_{l,k}} = \sum_{i,j} \frac{\partial \mathcal{L}}{\partial f_{l,i,j}} \frac{\partial f_{l,i,j}}{\partial \phi_{l,k}}, \quad (14)$$

$$\frac{\partial f_{l,i,j}}{\partial \phi_{l,k}} = \frac{1}{2} [f_{QC}(\phi_{l,k} + \pi/2) - f_{QC}(\phi_{l,k} - \pi/2)], \quad (15)$$

where $f_{l,i,j}$ denotes the neuron in the first hidden layer. Here, l represents the feature index, while i and j are spatial indices within each feature layer. The function $f_{QC}(\phi_k)$ is defined as

$$f_{QC}(\phi_k) = \langle \psi_{k-1} | U^\dagger(\phi_k) B_{k+1} U(\phi_k) | \psi_{k-1} \rangle, \quad (16)$$

where $U(\phi_k)$ is the single qubit operator associated with ϕ_k . The quantum state $|\psi_{k-1}\rangle$ is defined as

$$|\psi_{k-1}\rangle = U(\phi_{k-1}) \cdots U(\phi_1) V U(\theta_N) \cdots U(\theta_1) |0\rangle, \quad (17)$$

and the quantum operator B_{k+1} is defined as

$$B_{k+1} = U^\dagger(\phi_{k+1}) \cdots U^\dagger(\phi_N) W^\dagger Z^{\otimes N} W U^\dagger(\phi_N) \cdots U(\phi_{k+1}). \quad (18)$$

To simulate quantum circuits, we utilized Qulacs, a Python/C++ library with CPU and GPU supports⁷⁴. In this work, we considered 16 features in the first hidden layer. For different feature numbers, we direct readers to supplementary note 2.

Data Availability

The data that support the findings of this study are available from the corresponding authors upon reasonable request.

Code Availability

The code is available at <https://github.com/sli43/hybrid-quantum-classical-CNN>.

References

1. Ladd, T. D. *et al.* Quantum computers. *Nature* **464**, 45–53, DOI: [10.1038/nature08812](https://doi.org/10.1038/nature08812) (2011).
2. Cao, Y. *et al.* Quantum Chemistry in the Age of Quantum Computing. *Chem. Rev.* **119**, 10856–10915, DOI: [10.1021/acs.chemrev.8b00803](https://doi.org/10.1021/acs.chemrev.8b00803) (2019).
3. Liu, Y., Arunachalam, S. & Temme, K. A rigorous and robust quantum speed-up in supervised machine learning. *Nat. Phys.* **17**, 1013–1017, DOI: [10.1038/s41567-021-01287-z](https://doi.org/10.1038/s41567-021-01287-z) (2021).
4. Aaronson, S. & Chen, L. Complexity-Theoretic foundations of quantum supremacy experiments. *arXiv: 1612.05903* DOI: <https://arxiv.org/abs/1612.05903> (2016).
5. Klco, N. & Savage, M. J. Minimally entangled state preparation of localized wave functions on quantum computers. *Phys. Rev. A* **102**, 012612, DOI: [10.1103/PhysRevA.102.012612](https://doi.org/10.1103/PhysRevA.102.012612) (2020).
6. Niu, M. Y. *et al.* Entangling quantum generative adversarial networks. *Phys. Rev. Lett.* **128**, 220505, DOI: [10.1103/PhysRevLett.128.220505](https://doi.org/10.1103/PhysRevLett.128.220505) (2022).
7. O'Brien, J. L. Optical quantum computing. *Science* **218**, 1567–1570, DOI: [10.1126/science.1142892](https://doi.org/10.1126/science.1142892) (2007).
8. Jerbi, S. *et al.* Quantum machine learning beyond kernel methods. *Nat. Commun.* **14**, 517, DOI: [10.1038/s41467-023-36159-y](https://doi.org/10.1038/s41467-023-36159-y) (2023).
9. Sood, S. K. & Pooja. Quantum computing review: a decade of research. *IEEE Transactions on Eng. Manag.* 1–15, DOI: [10.1109/TEM.2023.3284689](https://doi.org/10.1109/TEM.2023.3284689) (2023).
10. Paine, A. E., Elfving, V. E. & Kyriienko, O. Quantum kernel methods for solving regression problems and differential equations. *Phys. Rev. A* **107**, 032428, DOI: [10.1103/PhysRevA.107.032428](https://doi.org/10.1103/PhysRevA.107.032428) (2023).
11. Kok, P. *et al.* Linear optical quantum computing with photonic qubits. *Rev. Mod. Phys.* **79**, 135–174, DOI: [10.1103/RevModPhys.79.135](https://doi.org/10.1103/RevModPhys.79.135) (2007).
12. Barends, R. *et al.* Superconducting quantum circuits at the surface code threshold for fault tolerance. *Nature* **508**, 500–503, DOI: [10.1038/nature13171](https://doi.org/10.1038/nature13171) (2014).
13. Ballance, C. J., Harty, T. P., Linke, N. M., Sepiol, M. A. & Lucas, D. M. High-Fidelity quantum logic gates using trapped-ion hyperfine qubits. *Phys. Rev. Lett.* **117**, 060504, DOI: [10.1103/PhysRevLett.117.060504](https://doi.org/10.1103/PhysRevLett.117.060504) (2016).
14. Georgescu, I. Trapped ion quantum computing turns 25, DOI: [10.1038/s42254-020-0189-1](https://doi.org/10.1038/s42254-020-0189-1) (2020).
15. Evered, S. J. *et al.* High-fidelity parallel entangling gates on a neutral-atom quantum computer. *Nature* 268–272, DOI: [10.1038/s41586-023-06481-y](https://doi.org/10.1038/s41586-023-06481-y) (2023).
16. Arute, F. *et al.* Quantum supremacy using a programmable superconducting processor. *Nature* **574**, 505–510, DOI: [10.1038/s41586-019-1666-5](https://doi.org/10.1038/s41586-019-1666-5) (2019).
17. Zhong, H.-S. *et al.* Quantum computational advantage using photons. *Science* **370**, 1460–1463, DOI: [10.1126/science.abe8770](https://doi.org/10.1126/science.abe8770) (2020).
18. Peruzzo, A. *et al.* A variational eigenvalue solver on a photonic quantum processor. *Nat. Commun.* **5**, 4213, DOI: [10.1038/ncomms5213](https://doi.org/10.1038/ncomms5213) (2014).

19. O'Malley, P. J. J. *et al.* Scalable quantum simulation of molecular energies. *Phys. Rev. X* **6**, 031007, DOI: [10.1103/PhysRevX.6.031007](https://doi.org/10.1103/PhysRevX.6.031007) (2016).
20. Kivlichan, I. D. *et al.* Quantum simulation of electronic structure with linear depth and connectivity. *Phys. Rev. Lett.* **120**, 110501, DOI: [10.1103/PhysRevLett.120.110501](https://doi.org/10.1103/PhysRevLett.120.110501) (2018).
21. Tubman, N. M. *et al.* Postponing the orthogonality catastrophe: efficient state preparation for electronic structure simulations on quantum devices, DOI: <https://arxiv.org/abs/1809.05523> (2018).
22. Dong, Y., Lin, L. & Tong, Y. Ground-State preparation and energy estimation on early fault-tolerant quantum computers via quantum eigenvalue transformation of unitary matrices. *PRX Quantum* **3**, 040305, DOI: [10.1103/PRXQuantum.3.040305](https://doi.org/10.1103/PRXQuantum.3.040305) (2022).
23. Qing, M. & Xie, W. Use VQE to calculate the ground energy of hydrogen molecules on IBM Quantum. *arXiv*: [2305.06538](https://arxiv.org/abs/2305.06538) DOI: <https://arxiv.org/abs/2305.06538> (2023).
24. Smith, A. W. R., Paige, A. J. & Kim, M. S. Faster variational quantum algorithms with quantum kernel-based surrogate models. *Quantum Sci. Technol.* **8**, 045016, DOI: [10.1088/2058-9565/aceb87](https://doi.org/10.1088/2058-9565/aceb87) (2023).
25. Bauer, B., Wecker, D., Millis, A. J., Hastings, M. B. & Troyer, M. Hybrid quantum-classical approach to correlated materials. *Phys. Rev. X* **6**, 031045, DOI: [10.1103/PhysRevX.6.031045](https://doi.org/10.1103/PhysRevX.6.031045) (2016).
26. Baker, T. E. Lanczos recursion on a quantum computer for the Green's function and ground state. *Phys. Rev. A* **103**, 032404, DOI: [10.1103/PhysRevA.103.032404](https://doi.org/10.1103/PhysRevA.103.032404) (2021).
27. Rizzo, J. *et al.* One-particle Green's functions from the quantum equation of motion algorithm. *Phys. Rev. Res.* **4**, 043011, DOI: [10.1103/PhysRevResearch.4.043011](https://doi.org/10.1103/PhysRevResearch.4.043011) (2022).
28. Li, Q., Cui, J. & Li, W. Detecting confined and deconfined spinons in dynamical quantum simulations. *Phys. Rev. Res.* **4**, 013193, DOI: [10.1103/PhysRevResearch.4.013193](https://doi.org/10.1103/PhysRevResearch.4.013193) (2022).
29. Mendes-Santos, T., Schmitt, M. & Heyl, M. Highly resolved spectral functions of two-dimensional systems with neural quantum states. *Phys. Rev. Lett.* **131**, 046501, DOI: [10.1103/PhysRevLett.131.046501](https://doi.org/10.1103/PhysRevLett.131.046501) (2023).
30. Farhi, E. *et al.* A quantum adiabatic evolution algorithm applied to random instances of an NP-complete problem. *Science* **292**, 472–475, DOI: [10.1126/science.1057726](https://doi.org/10.1126/science.1057726) (2001).
31. Hu, S., Liu, P., Chen, C.-F. R. & Pistoia, M. Automatically Solving NP-Complete Problems on a Quantum Computer. In *Proceedings of the 40th International Conference on Software Engineering: Companion Proceedings*, ICSE '18, 258–259, DOI: [10.1145/3183440.3194959](https://doi.org/10.1145/3183440.3194959) (Association for Computing Machinery, 2018).
32. Arrazola, J. M., Diamanti, E. & Kerenidis, I. Quantum superiority for verifying NP-complete problems with linear optics. *npj Quantum Inf.* **4**, 56, DOI: [10.1038/s41534-018-0103-1](https://doi.org/10.1038/s41534-018-0103-1) (2018).
33. Centrone, F., Kumar, N., Diamanti, E. & Kerenidis, I. Experimental demonstration of quantum advantage for NP verification with limited information. *Nat. Commun.* **12**, 850, DOI: [10.1038/s41467-021-21119-1](https://doi.org/10.1038/s41467-021-21119-1) (2021).
34. Zhang, A. *et al.* Quantum verification of NP problems with single photons and linear optics. *Light. Sci. & Appl.* **10**, 169, DOI: [10.1038/s41377-021-00608-4](https://doi.org/10.1038/s41377-021-00608-4) (2021).
35. Biamonte, J. *et al.* Quantum machine learning. *Nature* **549**, 195–202, DOI: [10.1038/nature23474](https://doi.org/10.1038/nature23474) (2017).
36. Ciliberto, C. *et al.* Quantum machine learning: a classical perspective. *Proc. Royal Soc. A: Math. Phys. Eng. Sci.* **474**, 20170551, DOI: [10.1098/rspa.2017.0551](https://doi.org/10.1098/rspa.2017.0551) (2018).
37. Schuld, M. Supervised quantum machine learning models are kernel methods. *arXiv*: [2101.11020](https://arxiv.org/abs/2101.11020) DOI: <https://arxiv.org/abs/2101.11020> (2021).
38. Blank, C., Park, D. K., Rhee, J.-K. K. & Petruccione, F. Quantum classifier with tailored quantum kernel. *npj Quantum Inf.* **6**, 41, DOI: [10.1038/s41534-020-0272-6](https://doi.org/10.1038/s41534-020-0272-6) (2020).
39. Zoufal, C., Lucchi, A. & Woerner, S. Quantum generative adversarial networks for learning and loading random distributions. *npj Quantum Inf.* **5**, 103, DOI: <https://doi.org/10.1038/s41534-019-0223-2> (2019).
40. Huang, K. *et al.* Quantum generative adversarial networks with multiple superconducting qubits. *npj Quantum Inf.* **7**, 165, DOI: [10.1038/s41534-021-00503-1](https://doi.org/10.1038/s41534-021-00503-1) (2021).
41. Tancara, D., Dinani, H. T., Norambuena, A., Fanchini, F. F. & Coto, R. Kernel-based quantum regressor models learning non-Markovianity. *Phys. Rev. A* **107**, 022402, DOI: [10.1103/PhysRevA.107.022402](https://doi.org/10.1103/PhysRevA.107.022402) (2023).
42. Slattery, L. *et al.* Numerical evidence against advantage with quantum fidelity kernels on classical data. *Phys. Rev. A* **107**, 062417, DOI: [10.1103/PhysRevA.107.062417](https://doi.org/10.1103/PhysRevA.107.062417) (2023).
43. Havlíček, V. *et al.* Supervised learning with quantum-enhanced feature spaces. *Nature* **567**, 209–212, DOI: [10.1038/s41586-019-0980-2](https://doi.org/10.1038/s41586-019-0980-2) (2019).
44. Pérez-Salinas, A., Cervera-Lierta, A., Gil-Fuster, E. & Latorre, J. I. Data re-uploading for a universal quantum classifier. *Quantum* **4**, 226, DOI: [10.22331/q-2020-02-06-26](https://doi.org/10.22331/q-2020-02-06-26) (2020).
45. Moreira, M. S. *et al.* Realization of a quantum neural network using repeat-until-success circuits in a superconducting quantum processor. *npj Quantum Inf.* **9**, 118, DOI: [10.1038/s41534-023-00779-5](https://doi.org/10.1038/s41534-023-00779-5) (2023).
46. Rebentrost, P., Mohseni, M. & Lloyd, S. Quantum support vector machine for big data classification. *Phys. Rev. Lett.* **113**, 130503, DOI: [10.1103/PhysRevLett.113.130503](https://doi.org/10.1103/PhysRevLett.113.130503) (2014).
47. Lloyd, S., Schuld, M., Ijaz, A., Izaac, J. & Killoran, N. Quantum embeddings for machine learning. *arXiv*: [2001.03622](https://arxiv.org/abs/2001.03622) DOI: <https://arxiv.org/abs/2001.03622> (2020).
48. Peters, E. *et al.* Machine learning of high dimensional data on a noisy quantum processor. *npj Quantum Inf.* **7**, 161, DOI: [10.1038/s41534-021-00498-9](https://doi.org/10.1038/s41534-021-00498-9) (2021).
49. Kusumoto, T., Mitarai, K., Fujii, K., Kitagawa, M. & Negoro, M. Experimental quantum kernel trick with nuclear spins in a solid. *npj Quantum Inf.* **7**, 94, DOI: [10.1038/s41534-021-00423-0](https://doi.org/10.1038/s41534-021-00423-0) (2021).
50. Jäger, J. & Krems, R. V. Universal expressiveness of variational quantum classifiers and quantum kernels for support vector machines. *Nat. Commun.* **14**, 576, DOI: [10.1038/s41467-023-36144-5](https://doi.org/10.1038/s41467-023-36144-5) (2023).

51. Alam, M., Kundu, S., Topaloglu, R. O. & Ghosh, S. Quantum-classical hybrid machine learning for image classification (iccad special session paper), DOI: [10.1109/ICCAD51958.2021.9643516](https://doi.org/10.1109/ICCAD51958.2021.9643516) (2021).

52. Trochun, Y. *et al.* Hybrid classic-quantum neural networks for image classification. In *2021 11th IEEE International Conference on Intelligent Data Acquisition and Advanced Computing Systems: Technology and Applications (IDAACS)*, vol. 2, 968–972, DOI: [10.1109/IDAACS5328.2021.9661011](https://doi.org/10.1109/IDAACS5328.2021.9661011) (2021).

53. Nakaji, K. *et al.* Approximate amplitude encoding in shallow parameterized quantum circuits and its application to financial market indicators. *Phys. Rev. Res.* **4**, 023136, DOI: [10.1103/PhysRevResearch.4.023136](https://doi.org/10.1103/PhysRevResearch.4.023136) (2022).

54. Ajlouni, N., Özyavaş, A., Takaoglu, M., Takaoglu, F. & Ajlouni, F. Medical image diagnosis based on adaptive hybrid quantum CNN. *BMC Med. Imaging* **23**, 126, DOI: [10.1186/s12880-023-01084-5](https://doi.org/10.1186/s12880-023-01084-5) (2023).

55. Yetis, H. & Karaköse, M. Variational quantum circuits for convolution and window-based image processing applications. *Quantum Sci. Technol.* **8**, 045004, DOI: [10.1088/2058-9565/ace378](https://doi.org/10.1088/2058-9565/ace378) (2023).

56. Zeguendry, A., Jarir, Z. & Quafafou, M. Quantum machine learning: a review and case studies. *Entropy* **25**, 287, DOI: [10.3390/e25020287](https://doi.org/10.3390/e25020287) (2023).

57. Rath, M. & Date, H. Quantum data encoding: a comparative analysis of classical-to-quantum mapping techniques and their impact on machine learning accuracy. *arXiv: 2311.10375* DOI: <https://arxiv.org/abs/2311.10375> (2023).

58. Gilyén, A., Lloyd, S. & Tang, E. Quantum-inspired low-rank stochastic regression with logarithmic dependence on the dimension. *arXiv: 1811.04909* (2018).

59. Chia, N.-H., Lin, H.-H. & Wang, C. Quantum-inspired sublinear classical algorithms for solving low-rank linear systems. *arXiv: 1811.04852* DOI: <https://arxiv.org/abs/1811.04852> (2018).

60. Arrazola, J. M., Delgado, A., Bardhan, B. R. & Lloyd, S. Quantum-inspired algorithms in practice. *Quantum* **4**, 307, DOI: <https://doi.org/10.22331/q-2020-08-13-307> (2020).

61. Tang, E. Quantum principal component analysis only achieves an exponential speedup because of its state preparation assumptions. *Phys. Rev. Lett.* **127**, 060503, DOI: [10.1103/PhysRevLett.127.060503](https://doi.org/10.1103/PhysRevLett.127.060503) (2021).

62. Hwang, W., Park, D. K., Araujo, I. F. & Blank, C. Quantum-inspired classification via efficient simulation of helstrom measurement. *arXiv: 2403.15308* DOI: <https://arxiv.org/abs/2403.15308> (2024).

63. Sim, S., Johnson, P. D. & Aspuru-Guzik, A. Expressibility and Entangling Capability of Parameterized Quantum Circuits for Hybrid Quantum-Classical Algorithms. *Adv. Quantum Technol.* **2**, 1900070, DOI: <https://onlinelibrary.wiley.com/doi/abs/10.1002/qute.201900070> (2019).

64. Schuld, Maria and Bocharov, Alex and Svore, Krysta M. and Wiebe, Nathan. Circuit-centric quantum classifiers. *Phys. Rev. A* **101**, 032308, DOI: [10.1103/PhysRevA.101.032308](https://doi.org/10.1103/PhysRevA.101.032308) (2020).

65. Du, Y., Hsieh, M.-H., Liu, T. & Tao, D. Expressive power of parametrized quantum circuits. *Phys. Rev. Res.* **2**, 033125, DOI: [10.1103/PhysRevResearch.2.033125](https://doi.org/10.1103/PhysRevResearch.2.033125) (2020).

66. Wu, Y., Yao, J., Zhang, P. & Li, X. Randomness-Enhanced expressivity of quantum neural networks. *Phys. Rev. Lett.* **132**, 010602, DOI: [10.1103/PhysRevLett.132.010602](https://doi.org/10.1103/PhysRevLett.132.010602) (2024).

67. McClean, J. R., Boixo, S., Smelyanskiy, V. N., Babbush, R. & Neven, H. Barren plateaus in quantum neural network training landscapes. *Nat. Commun.* **9**, 4812, DOI: [10.1038/s41467-018-07090-4](https://doi.org/10.1038/s41467-018-07090-4) (2018).

68. Holmes, Z., Sharma, K., Cerezo, M. & Coles, P. J. Connecting ansatz expressibility to gradient magnitudes and barren plateaus. *PRX Quantum* **3**, 010313, DOI: [10.1103/PRXQuantum.3.010313](https://doi.org/10.1103/PRXQuantum.3.010313) (2022).

69. LeCun, Y., Cortes, C. & Burges, C. MNIST handwritten digit database. *ATT Labs* **2**, DOI: <http://yann.lecun.com/exdb/mnist> (2010).

70. Ju, Y.-L., Tsai, I.-M. & Kuo, S.-Y. Quantum circuit design and analysis for database search applications. *IEEE Transactions on Circuits Syst. I: Regul. Pap.* **54**, 2552–2563, DOI: [10.1109/TCSI.2007.907845](https://doi.org/10.1109/TCSI.2007.907845) (2007).

71. Du, Y., Huang, T., You, S., Hsieh, M.-H. & Tao, D. Quantum circuit architecture search for variational quantum algorithms. *npj Quantum Inf.* **8**, 62, DOI: [10.1038/s41534-022-00570-y](https://doi.org/10.1038/s41534-022-00570-y) (2022).

72. Hoefer, T., Haener, T. & Troyer, M. Disentangling hype from practicality: on realistically achieving quantum advantage. *arXiv: 2307.00523* DOI: <https://arxiv.org/abs/2307.00523> (2023).

73. Crooks, G. E. Gradients of parameterized quantum gates using the parameter-shift rule and gate decomposition, DOI: <https://arxiv.org/abs/1905.13311> (2019).

74. Suzuki, Y. *et al.* Qulacs: a fast and versatile quantum circuit simulator for research purpose. *Quantum* **5**, 559, DOI: [10.22331/q-2021-10-06-559](https://doi.org/10.22331/q-2021-10-06-559) (2021).

Acknowledgements

This work is supported by the National Center for Transportation Cybersecurity and Resiliency (TraCR) (a U.S. Department of Transportation National University Transportation Center) headquartered at Clemson University, Clemson, South Carolina, USA. Any opinions, findings, conclusions, and recommendations expressed in this material are those of the author(s) and do not necessarily reflect the views of TraCR. The U.S. Government assumes no liability for the contents or use thereof.

Author contributions

S.L. led this project, implemented codes, and performed simulations. All authors contribute to the discussion and writing the manuscript.

Competing interests

The authors declare no competing interests.

Additional Information

Supplementary Information accompanies this paper at [Insert_link](#).

Correspondence and requests for materials should be addressed to S.L.